



**Additive-free Molecular Acceptor Organic Solar Cells
Processed from a Biorenewable Solvent Approaching 15%
Efficiency**

Journal:	<i>Materials Horizons</i>
Manuscript ID	MH-COM-07-2023-001133.R2
Article Type:	Communication
Date Submitted by the Author:	28-Sep-2023
Complete List of Authors:	<p>Du, Zhifang; UCSB, Chemistry Luong, Hoang; University of California Santa Barbara, Sabury, Sina; Georgia Institute of Technology, Chemistry Therdkatanyuphong, Pattarawadee; University of Colorado Boulder Chae, Sangmin; UCSB, Chemistry and Biochemistry Welton, Claire; University of Lille Jones, Austin; Georgia Institute of Technology, Chemistry and Biochemistry Zhang, Junxiang; University of Colorado Boulder Peng, Zhengxing; North Carolina State University, Zhu, Ziyue; University of California Santa Barbara, Chemistry and Biochemistry Nanayakkara, Sadisha; The University of Arizona, Chemistry and Biochemistry Coropceanu, Veaceslav; The University of Arizona, Chemistry and Biochemistry Choi, Dylan; University of California Santa Barbara Xiao, Steven; 1-material, Yi, Ahra; University of California Santa Barbara, Chemistry and Biochemistry Kim, Hyo Jung; Pusan National University, Department of Organic Material Science and Engineering Bredas, Jean-Luc ; University of Arizona, Chemistry and Biochemistry Ade, Harald; North Carolina State University, Department of Physics Manjunatha Reddy, G.; University of Lille, Chemistry; Northwestern University, Chemistry Marder, Seth; University of Colorado Boulder, Chemistry; University of Colorado Boulder, Renewable and Sustainable Energy Institute; Georgia Institute of Technology, School of Chemistry and Biochemistry Reynolds, John; Georgia Institute of Technology, Chemistry and Biochemistry, Materials Science and Engineering Nguyen, Thuc-Quyen; University of California, Santa Barbara, Chemistry and Biochemistry</p>

SCHOLARONE™
Manuscripts

1 **Additive-free Molecular Acceptor Organic Solar Cells Processed from a Biorenewable**
2 **Solvent Approaching 15% Efficiency**

3
4 *Zhifang Du*¹, *Hoang Mai Luong*¹, *Sina Sabury*², *Pattarawadee Therdkatanyuphong*³, *Sangmin*
5 *Chae*¹, *Claire Welton*⁴, *Austin L. Jones*², *Junxiang Zhang*³, *Zhengxing Peng*⁵, *Ziyue Zhu*¹, *Sadisha*
6 *Nanayakkara*⁶, *Veaceslav Coropceanu*⁶, *Dylan G. Choi*¹, *Steven Xiao*⁷, *Ahra Yi*^{1,8}, *Hyo Jung Kim*⁸,
7 *Jean-Luc Bredas*⁶, *Harald Ade*⁵, *G. N. Manjunatha Reddy*^{4*}, *Seth R. Marder*^{3*}, *John R. Reynolds*^{2*},
8 *Thuc-Quyen Nguyen*^{1*}

9
10 ¹ Center for Polymers and Organic Solids, Department of Chemistry and Biochemistry,
11 University of California at Santa Barbara, Santa Barbara, CA, 93106, USA

12
13 ² School of Chemistry and Biochemistry, School of Materials Science and Engineering, Center for
14 Organic Photonics and Electronics, Georgia Tech Polymer Network, Georgia Institute of
15 Technology, Atlanta, Georgia 30332, United States

16
17 ³ University of Colorado Boulder, Renewable and Sustainable Energy Institute, Boulder, CO
18 80303, USA

19
20 ⁴ University of Lille, CNRS, Centrale Lille Institut, Univ. Artois, UMR 8181, Unité de Catalyse et
21 Chimie du Solide, F-59000, Lille, France

22
23 ⁵ Department of Physics and Organic and Carbon Electronics Laboratories (ORaCEL), North
24 Carolina State University, Raleigh, NC 27695, USA

25
26 ⁶ Department of Chemistry and Biochemistry, The University of Arizona, Tucson, AZ, 85721-
27 0088, USA

28
29 ⁷ 1-Material Inc, 2290 Chemin St-Francois, Dorval, Quebec, H9P 1K2, Canada
30

1 ⁸ Department of Organic Material Science and Engineering, School of Chemical Engineering,
2 Pusan National University, Busan 46241, Republic of Korea

3
4 *Corresponding Author Emails: quyen@chem.ucsb.edu, reynolds@chemistry.gatech.edu,
5 sema1789@colorado.edu, gnm.reddy@univ-lille.fr

6
7 Keywords: conjugated polymers, molecular acceptors, environmental sustainability, green solvent
8 processing, organic photovoltaics, bulk heterojunction morphology, solid-state NMR

9

10

11 **New concepts**

12 Recent upsurge in the solar-to-electrical power conversion efficiency (PCE) associated with
13 organic photovoltaics (OPVs) opens up new opportunities, particularly by means of their
14 commercial viability. However, several challenges must be overcome. Among others,
15 processability of OPVs using green-solvents without compromising much on the performance is
16 paramount. This study makes use of newly designed small molecular acceptors (MAs) and donor
17 polymers processed with a *biomass-derived solvent* (2-methyltetrahydrofuran, 2-MeTHF) to
18 facilitate high performance of ~15% PCE in bulk heterojunction (BHJ) OPVs without using
19 halogenated additives. In doing so, this work provides unprecedented new insights into the
20 molecular origins of moderate-to-high PCEs in the 9-15% range for the BHJ OPVs processed from
21 2-Me THF. The synergism between synthesis, processing, characterization and device physics is
22 used to explain the rationale for the large variation in the PCE values. This is further corroborated
23 by morphology analysis at different length scales using microscopy, X-ray scattering and magnetic
24 resonance spectroscopy techniques, which indicate that the domain size and purity, D-A intermix
25 and distribution, and local packing interactions facilitate high performance in 'green' OPVs.

26

1 **Abstract**

2 We report on the use of molecular acceptors (MAs) and donor polymers processed with a biomass-
3 derived solvent (2-methyltetrahydrofuran, 2-MeTHF) to facilitate bulk heterojunction (BHJ)
4 organic photovoltaics (OPVs) with power conversion efficiency (PCE) approaching 15%. Our
5 approach makes use of two newly designed donor polymers with an opened ring unit in their
6 structures and of three molecular acceptors (MAs) where the backbone and sidechain were
7 engineered to enhance the processability of BHJ OPVs using 2-MeTHF, as evaluated by an
8 analysis of donor-acceptor (D-A) miscibility and interaction parameters. To understand the
9 differences in the PCE values that ranged from 9-15% as a function of composition, the surface,
10 bulk, and interfacial BHJ morphologies were characterized at different length scales using atomic
11 force microscopy, grazing-incidence wide-angle X-ray scattering, resonant soft X-ray scattering,
12 X-ray photoelectron spectroscopy, and 2D solid-state nuclear magnetic resonance spectroscopy.
13 Our results indicate that the favorable D-A intermixing that occurs in the best performing BHJ
14 film with an average domain size of ~25 nm, high domain purity, uniform distribution and
15 enhanced local packing interactions— facilitates charge generation and extraction while limiting
16 the trap-assisted recombination process in the device, leading to highly effective mobility and good
17 performance.

1 **1. Introduction**

2 The continued push to optimize the properties associated with organic photovoltaic (OPV) cells
3 has enabled high power conversion efficiencies (PCEs) approaching 20%, which can help
4 encourage and facilitate the commercialization of devices based upon these materials.¹⁻⁴ Most
5 high-performance single junction OPV devices are processed from halogenated solvents such as
6 chloroform (which is highly volatile) (CF), chlorobenzene (CB), and additives such as 1,8-
7 diiodooctane (DIO) and 1-chloronaphthalene (CN),^{5,6} which are hazardous to either human health
8 or the environment, or both. Therefore, the use of such solvents (and additives) is an impediment
9 to the large-scale commercialization of OPV modules and it is desirable to replace them with eco-
10 friendly ‘green’ solvents generated from renewable agricultural resources.^{7, 8} However, there
11 usually is a trade-off between the use of these renewable solvents and PCE, and the development
12 of high-efficiency OPVs processed from green solvents necessitates new molecular design and
13 BHJ processing approaches, as well as a comprehensive understanding of structure-property
14 relationships. In this work, we focus on developing processable high-performance OPV BHJs,
15 using an environmentally friendly and sustainable solvent 2-methyltetrahydrofuran (2-MeTHF).

16 Although a large pool of non-halogenated solvents is available for processing of donor-
17 acceptor molecules and their blends, *a priori*, screening of potential solvents can be obtained based
18 on solubility, polarity, and dispersion, for example, by examining Hansen solubility parameters
19 (HSP).⁹⁻¹² Additives as morphology boosters also have a significant impact on the processability,
20 efficiency, and stability of OPVs.¹³⁻²² Regarding the use of non-halogenated solvents for
21 processing BHJ solar cells, *ortho*-xylene (*o*-xylene),²³⁻²⁷ toluene,^{26, 28} tetrahydrofuran (THF),²⁹
22 terpene bio-solvents,⁸ and 2-MeTHF have been reported. Among these solvents, 2-MeTHF is
23 produced from agriculture byproducts and widely utilized for large-scale organic synthesis in
24 industry.^{30, 31} Furthermore, it has a low boiling point (78 °C) allowing for fast drying and

1 processing BHJ mixtures into thin films³² for OPVs.^{28, 33-38} For example in early work, 2-MeTHF
2 treated BHJ-based OPVs involving a low bandgap polymer PPDPP and the PC₇₁BM acceptor
3 enabled a PCE of 4.18%.³⁴ In addition, an all-polymer solar cell consisting of the PTzBI-Si donor
4 and N2200 acceptor processed in non-halogenated solvents such as 2-MeTHF and cyclopentyl
5 methyl ether (CPME) resulted in a PCE of ~11%.³³ Very recently, the utility of 2-MeTHF as a
6 processing solvent is exemplified by work published during the preparation of this manuscript,
7 where PTQ10 and FO6-T polymer donors blended with Y12 acceptor were used to attain OPV
8 with up to 14.5% and 11.4% PCE.³⁵ Often, poor solubility of high-performance donor and acceptor
9 molecules in non-halogenated solvents such as *o*-xylene and 2-MeTHF is a bottleneck for
10 processing these molecules into BHJ thin films. Therefore, a considerable “molecular redesign” of
11 the donor/acceptor components is necessary to achieve good solubility in 2-MeTHF. This
12 enhanced miscibility and processability while keeping optimal film morphology for charge
13 generation and transport properties at the desired levels, which are crucial to formulate high-
14 performance BHJ thin films. Understanding the molecular origins of the factors that influence the
15 molecule packing in the BHJ morphology is important, as well as their role in governing device
16 performance, which is yet to be addressed and compared for OPVs processed from 2-MeTHF.

17 In this work, we designed a series of donor:acceptor (D:A) blends based on the PM7 series of
18 polymer donors with different backbone structures and Y-series molecule acceptors (MAs), in
19 which the position of the sidechains on the polymer and the alkyl chain length on the MAs are
20 used to control the solubility in 2-MeTHF without the use of additives. The replacement of the
21 closed-ring diketone in PM6 and PM7 with an opened ring diester quaterthiophene moiety in PM7-
22 D3 and PM7-D5 (structures are shown in **Figure 1a**) provides backbone flexibility. A combination
23 of characterization techniques is employed to resolve the BHJ morphology at different length

1 scales ranging from sub-nanometer to micrometer distances using solid-state nuclear magnetic
2 resonance spectroscopy (ssNMR), atomic force microscopy (AFM), grazing-incidence wide-angle
3 X-ray scattering (GIWAXS), and resonant soft x-ray scattering (RSoXS) techniques. In addition,
4 we characterized the optical properties, energetics, and electronic parameters that contribute to the
5 different PCE values in these BHJ devices. The *additive-free* donor and MA blended PM7-
6 D3:PTI04 device processed from 2-MeTHF demonstrates a PCE value of 14.9%, which is akin to
7 PM6:Y6 reference devices³⁹ processed from CF with additives. Our studies of the bulk and
8 interfacial BHJ morphology indicate that a favorable intermixing of PM7-D3 and PTI04 results in
9 appropriate MA domain sizes and phase purity. Furthermore, PM7-D3:PTI04 devices have high
10 charge carrier mobilities and low charge recombination, enabling high PCEs. Our studies suggest
11 that the underlying reasons for the lower performance of the other PM7-D5/PM7-D3:MA blends
12 (PCEs in the 9-11% range) are an unfavorable local morphology, which we attribute to the
13 positions of the ester sidechains on the donor polymers and elongated sidechains on the MAs.

14

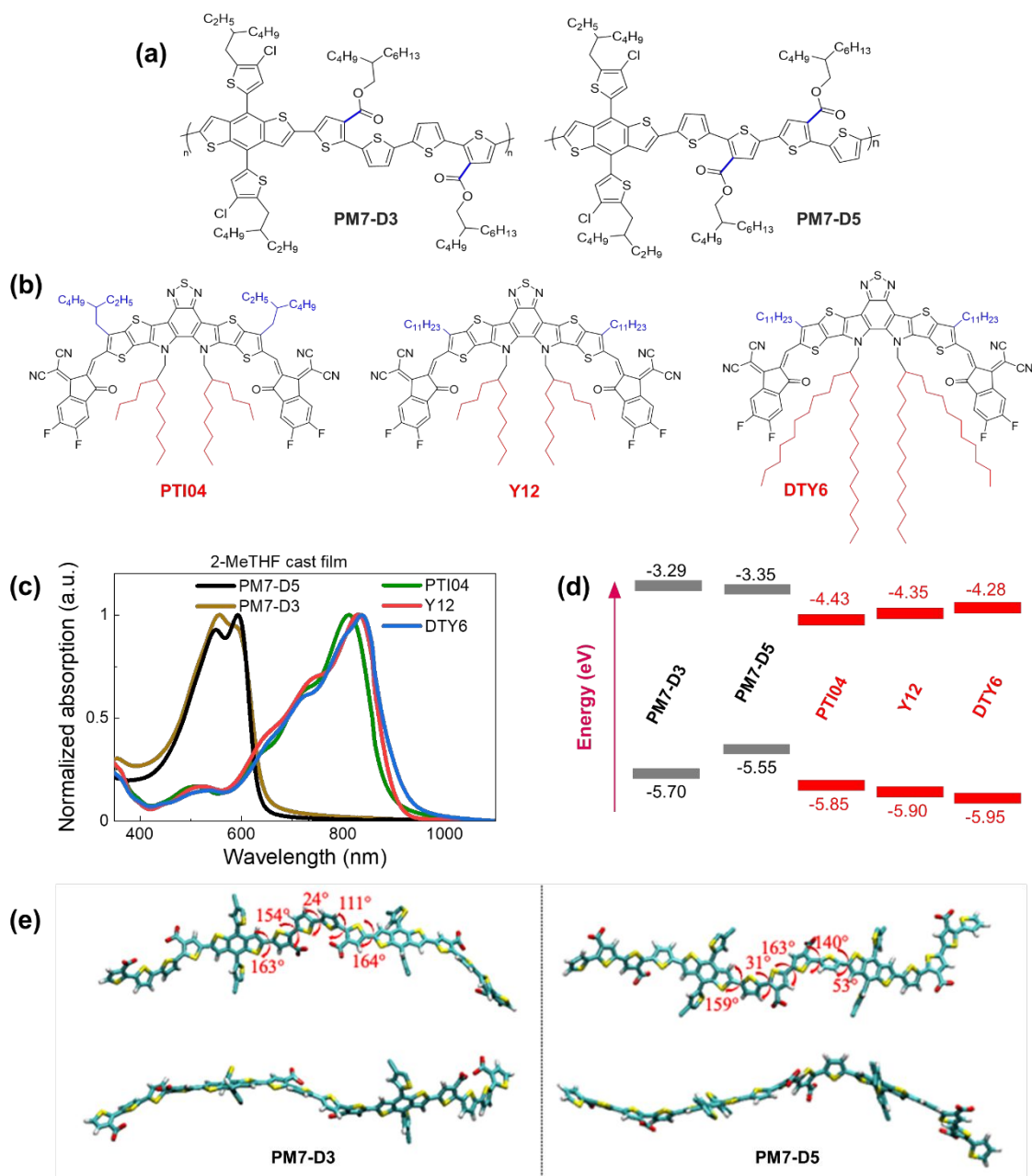
1 **2. Results and discussion**

2 **2.1. Molecular design, D-A interaction parameters, and optical properties**

3 The repeat unit structures of polymer donors (PM7-D3 and PM7-D5), which differ only in the
4 positions of the ester side chains on the thiophene rings of the backbone, and the structures of the
5 Y-series MAs (Y12, DTY6, and PTI04) with different sidechain lengths and branching are shown
6 in **Figures 1a** and **1b**. The synthesis of these polymers is simpler than the well-known high-
7 performance polymers PM6 and PM7. From gel permeation chromatography (Figure S8), PM7-
8 D3 has a higher molecular weight than PM7-D5 (M_n : 65 kg/mol, M_w : 149 kg/mol, \bar{D} : 2.30 versus
9 M_n : 26.1 kg/mol, M_w : 55 kg/mol, \bar{D} : 2.09). More details of the material synthesis and molecular
10 characterization are given in the Supporting Information (SI).

11 A comparison of the optical properties of neat donor polymer and MA thin films spin coated from
12 2-MeTHF solutions is given in **Figure 1c**, while their ionization energies (IEs) and electron
13 affinities (EAs) are shown in **Figure 1d**. The IE and EA energies are estimated based on the
14 extraction of the onset potentials using dynamic pulse voltammetry (DPV) versus
15 ferrocene/ferrocenium (considering a conversion factor of -5.12 V *vs.* vacuum). To better
16 represent solid-state characteristics and minimize any alterations in the film properties caused by
17 electrolyte absorption, the initial voltammograms of fresh films are employed, and different films
18 are utilized for the oxidation and reduction processes, so the onset for oxidation and reduction is
19 not affected by the electrochemical history (**Figures 1d**). A small variation in the IEs is observed,
20 which may be attributed to different aggregation and packing behaviors, as will be thoroughly
21 investigated below (*vide infra*).

22



1
2 **Figure 1.** Chemical structures of (a) PM7-D3 and PM7-D5, and (b) PTI04, Y12, and DTY6.
3 (c) Normalized absorption of thin films processed from 2-MeTHF. (d) Energy level diagram
4 of polymers donors and acceptors. (e) Top and side views of the optimized geometries (at the
5 ω B97X-D/6-31G(d, p) level of theory) for the symmetric dimeric models of **PM7-D3** (left),
6 and **PM7-D5** (right) polymers. The dihedral angles between selected moieties are indicated in
7 red. The long sidechains are omitted for clarity.

1 The degree of assembly of the D-polymer or MA in the BHJ blend can be influenced by their
2 solubility and aggregation tendency, which strongly depends on the backbone structures and
3 sidechains. For instance, when a D-polymer is blended with a MA, the delayed solidification of
4 the D-polymer results in a less favorable final morphology of the BHJ blend.⁴⁰ While enhancing
5 backbone planarity in conjugated polymers by utilizing fused aromatic rings is expected to
6 improve transport properties and device performance, these fused-ring-core polymers may lead to
7 reduced solubility and bring additional challenges to processability. Conversely, incorporating
8 flexible connections (non-fused rings) into the backbone often leads to enhanced solubility, but
9 the OPV performance may be compromised. By tailoring the backbone structure using fused ring
10 (benzodithiophene part) and non-fused ring (diester quaterthiophene part) components in PM7-D3
11 and PM7-D5, together with the placement of the branched 2-butyloctyl sidechains on the ester
12 functionalities, solubility in the green solvent 2-MeTHF can be adjusted and enhanced. The
13 presence of two peaks or a peak-shoulder pattern in the absorption spectrum of both PM7-D3 and
14 PM7-D5, respectively, suggests the presence of aggregates resulting from interchain π - π stacking.
15 In particular, the larger 0-0/0-1 ratio (ratio between the absorbance of shoulder to main peak) in
16 PM7-D5 points to a more planar backbone compared to PM7-D3.⁴¹ This observation is further
17 supported by the 150 meV lower IE for PM7-D5 and the results of long-range corrected ω B97X-
18 D/6-31G(d, p) density-functional theory (DFT) calculations based on symmetric dimers (**Figure**
19 **1e**), where the PM7-D5 backbone conformation intrinsically exhibits a higher degree of planarity.

20 For the donor polymers, backbone flexibility in PM7-D3 and PM7-D5 provides the requisite
21 solubility for processing films without compromising solid-state packing. PM7-D3 exhibits
22 solubility of slightly greater than 10 mg/mL in 2-MeTHF while PM7-D5 shows a slightly lower
23 solubility of approximately 7 mg/mL even at lower molecular weight, in line with the backbone

1 planarity trend between the two polymers. While molecular weight differences between the two
2 polymers can also play a role, the main factor contributing to the different solubilities and
3 aggregation behaviors between these two structural isomeric polymers is believed to be the
4 position of the diester sidechains in the quaterthiophene building block. One would expect PM7-
5 D5 rather than PM7-D3 to have a higher solubility in 2-MeTHF if only considering the low
6 molecular weight of PM7-D5. Thus, it is evident that the sidechain position in these polymers
7 controls the conformation of the backbone as corroborated by the DFT calculations for symmetric
8 dimers shown in **Figure 1e**. The enhanced conformational degrees of freedom and less planar
9 backbones in PM7-D3 coming from the position of the diester quaterthiophene are expected to
10 contribute to the improved solubility in 2-MeTHF. It is worth noting that all three MAs also
11 exhibited good processing capabilities with high solubility of ~10 mg/ml in eco-friendly solvent
12 2-MeTHF. For three MAs, similar high solubility of above 10 mg/mL in 2-MeTHF is observed,
13 which is also supported by a solubility assessment that describes the origins of good solubility
14 supported by Hansen solubility parameters (HSP). The HSP theory can evaluate the cohesive
15 energy density (CED) of material/solvent considering the contribution of dispersivity, polarity,
16 and hydrogen bonding togetherly.^{8, 11, 12} From the CEDs of selected molecules and solvents, the
17 molecule–solvent interaction parameters, χ , are calculated and summarized in the SI (Section 2,
18 Tables S2 and S3). Smaller χ values of around 0.70 indicate small differences in the properties
19 between three MAs and the host solvent, which further supports their good solubility in 2-MeTHF.
20 Thus, PM7-Dx:MA blends are highly versatile to the processability with 2-MeTHF.

21 **2.2. Photovoltaic characteristics**

22 To assemble OPV cells, the PM7-Dx:MA in a 1:1.2 weight ratio BHJ active layer was cast from
23 2-MeTHF heated at 70 °C to accelerate the drying of the thin films during spin coating,⁴² and the

1 resulting devices were tested. It is noteworthy that solvent additives were not used in order to
 2 eliminate the health and environmental hazards due to halogenated additives, which also simplifies
 3 the fabrication process for large-scale fabrication compatibility.^{20, 43} The device structure of
 4 ITO/PEDOT:PSS/PM7-Dx:MA/PNDIT-F3N-Br/Ag was utilized and a more detailed description
 5 of the device fabrication procedure can be found in the SI, Section 3. The current density-voltage
 6 (J - V) characteristics of these solar cells are shown in **Figure 2a** and **Table 2**. Due to this variation
 7 in IE values, it is expected that the PM7-D3 donor polymer with a higher IE (roughly speaking, a
 8 lower HOMO) can enhance the open-circuit voltage (V_{oc}) of the PM7-D3:MA OPV device relative
 9 to PM7-D5:MA BHJ. Among the four BHJ blends with different combinations of the donor
 10 polymers and the MAs, we found the highest PCE of $14.91 \pm 0.25\%$ for the PM7-D3:PTI04 device,
 11 enabled by a relatively high fill factor, FF (0.69), V_{oc} (0.90 V), and J_{sc} (23.88 mA cm^{-2}), which is
 12 also one of the best performing systems processing with 2-MeTHF compared to recent eco-friendly
 13 solvent treated organic solar cells shown in Table S4. The integration of the external quantum
 14 efficiency (EQE) spectrum, **Figure 2b**, results in a similar J_{sc} value for this system. By comparison,
 15 the other BHJ systems exhibited lower PCE values in the 9.61-11.28% range. We attribute this to
 16 the relatively large domain size and uneven distribution of donor and acceptor in the BHJ
 17 morphology of those devices, which will be further described by characterizing the photophysical
 18 parameters as well as performing a morphology analysis at different length scales.

19

20 **Table 1.** Photovoltaic parameters of the studied OPVs measured under simulated AM1.5G
 21 illumination. Average values are obtained from 10 devices.

Solvent	D:A	J_{sc} (mA cm^{-2})	V_{oc} (V)	FF	PCE_{avg} (%)
---------	-----	----------------------------------	--------------	------	-------------------------------

	PM7-D3: PTI04	23.88 ± 0.12	0.90 ± 0.01	0.69 ± 0.01	14.91 ± 0.25
	PM7-D3: Y12	23.76 ± 0.61	0.86 ± 0.01	0.54 ± 0.02	11.06 ± 0.49
2-MeTHF	PM7-D3: DTY6	20.29 ± 0.37	0.86 ± 0.01	0.65 ± 0.02	11.28 ± 0.35
	PM7-D5 :PTI04	17.17 ± 0.51	0.87 ± 0.01	0.64 ± 0.02	9.61 ± 0.45

1

2 To gain a deeper understanding of the device performance, we studied the voltage-dependent
3 charge collection probability (P_c) using the following equation,

$$4 \quad P_c = \frac{J_{\text{ph}}}{J_{\text{ph,sat}}}, \quad (1)$$

5

6 where the photocurrent density (J_{ph}) of the device is the difference between the current density
7 under illumination and in the dark,^{4, 44} and $J_{\text{ph,sat}}$ is the saturated photocurrent density under -2 V.

8 A high $J_{\text{ph,sat}}$ above 20 mA cm^{-2} and weak voltage-dependent P_c for all three PM7-D3:MA blends

9 indicate an efficient charge carrier generation rate in all devices. In **Figure 2c**, the P_c is plotted as

10 a function of the effective voltage ($V_{\text{eff}} = V_0 - V_{\text{cor}}$), where V_0 is the voltage at which J_{ph} equals

11 0, and the corrected voltage ($V_{\text{cor}} = V_{\text{app}} - JR_s$) is obtained by considering the voltage losses due

12 to series resistance (R_s). Under short-circuit condition (black line, **Figure 2c**), the PM7-D3:PTI04

13 device shows $P_c = 0.994$, which is the highest among the four systems characterized here. In other

14 words, the PM7-D3:PTI04 system has the most efficient charge collection process without the

15 assistance of the external electric field for charge extraction.

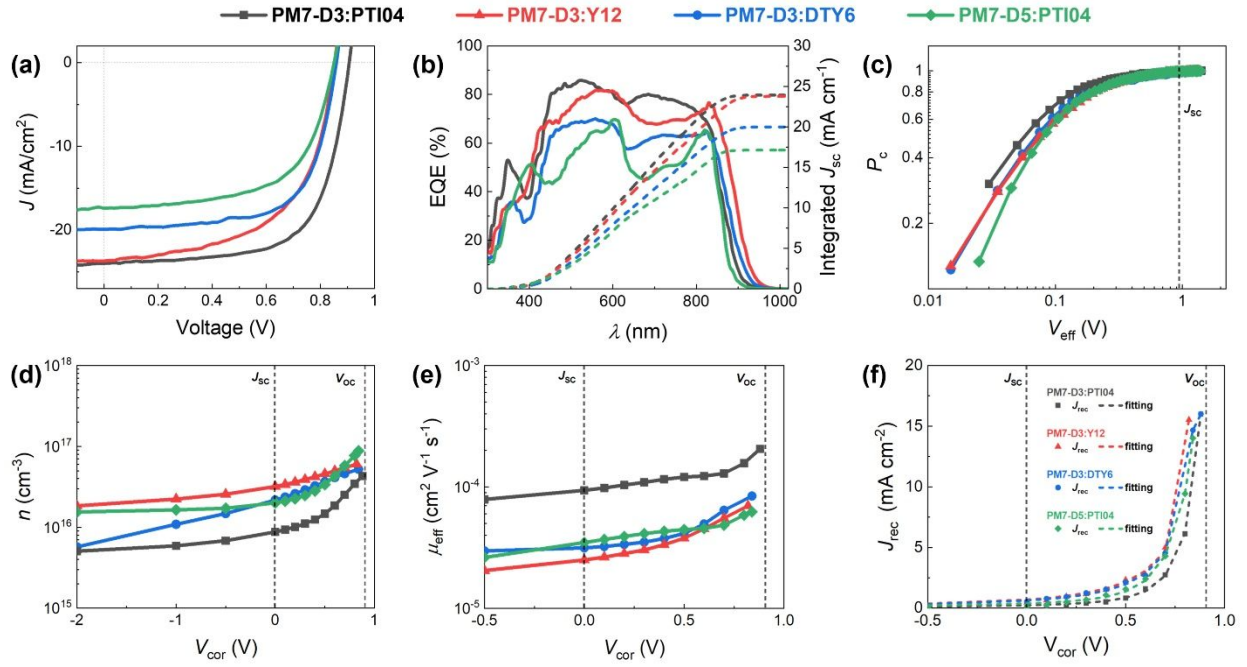


Figure 2. (a) J - V characteristics, (b) EQE spectra, (c) charge collection probability, (d) voltage-dependent charge carrier density, (e) voltage-dependent effectivity mobility, and (f) fitting of the recombination current density of PM7-D3:PTI04, PM7-D3:Y12, PM7-D3:DTY6, and PM7-D5:PTI04 under AM1.5G illumination at 100 mW cm^{-2} .

Next, impedance spectroscopy was carried out to determine the charge carrier density in the active layer upon varying operational biases and light intensities.⁴⁵⁻⁵² To maintain the steady-state properties of the system during measurement under different illumination conditions, DC bias in a range from -2 V to V_{oc} , and a small AC signal (40 mV) were applied during the scanning. To account for the impact of the device series resistance and parasitic inductance of the connecting cables, a correction factor is included in the measured capacitance of the BHJ layer as represented in Equation (2):

$$C_{cor} = -\frac{1}{\omega} \left[\frac{Z'' - \omega L'}{(Z' - R_s)^2 + (Z'' - \omega L')^2} \right], \quad (2)$$

1 Here, L' is the inductance of the connecting cables, $\omega = 2\pi\nu$ is the angular frequency of the
 2 AC signal, and Z' and Z'' are the real and imaginary components of impedance, respectively. In the
 3 dark, the corrected capacitance measured under a large reverse bias (-2 V) shows a horizontal line,
 4 which is equivalent to a frequency-independent capacitance. From this, one can determine the
 5 geometrical capacitance (C_g) of the active layer. Voltage-dependent impedance spectroscopy
 6 measurements were performed to obtain the charge carrier density n (**Figure 2d**), via integration
 7 of the chemical capacitance C_{chem} using the following equations:^{24, 46, 53-55}

$$8 \quad n(V_{\text{cor}}) = n_{\text{sat}} + \frac{1}{qAL} \int_{V_{\text{sat}}}^{V_{\text{cor}}} C_{\text{chem}} dV_{\text{cor}}, \quad (3)$$

$$9 \quad n_{\text{sat}} = \frac{1}{qAL} C_{\text{sat}} (V_0 - V_{\text{sat}}), \quad (4)$$

10 where V_0 is the forward bias at which the photocurrent is equal to zero, A is the device area (9.4
 11 mm^2), L is the thickness of the active layer, V_{sat} is the reverse bias at which the photocurrent
 12 saturates (-2 V), and C_{sat} is the internal capacitance, which is determined by the difference of the
 13 corrected capacitance in the dark and under illumination at V_{sat} . The charge carrier density in the
 14 range from -2 V to close to V_{oc} under 100 mW cm^{-2} illumination in PM7-D3:PTI04 devices shows
 15 an overall lower value ($n < 1.6 \times 10^{16} \text{ cm}^{-3}$) than that in other devices ($n > 2.5 \times 10^{16} \text{ cm}^{-3}$), while
 16 the effective mobility μ_{eff} ($1.1 \times 10^{-4} \text{ cm}^2 \text{ V}^{-1} \text{ s}^{-1}$) is about one order of magnitude higher than in
 17 the other devices ($< 3.5 \times 10^{-5} \text{ cm}^2 \text{ V}^{-1} \text{ s}^{-1}$); μ_{eff} is calculated using the following equation:

$$18 \quad \mu_{\text{eff}}(n, V_{\text{cor}}) = \frac{J(V)L}{2qn(V)[V_{\text{oc}} - V_{\text{cor}}]}, \quad (5)$$

19 where V_{cor} is the corrected voltage considering the voltage drop over the series resistance, and J
 20 (V) is the current density obtained from the J - V curves. The higher charge carrier mobility in the
 21 PM7-D3:PTI04 can improve the collection process, leading to a small remaining amount of free

1 charge carriers in the BHJ layer, which agrees with the minimum average $n(V)$ in the operating
 2 range from -2 V to a bias 0.2 V lower than V_{oc} . Among the other factors that influence the PCE
 3 values are the recombination dynamics and voltage losses.

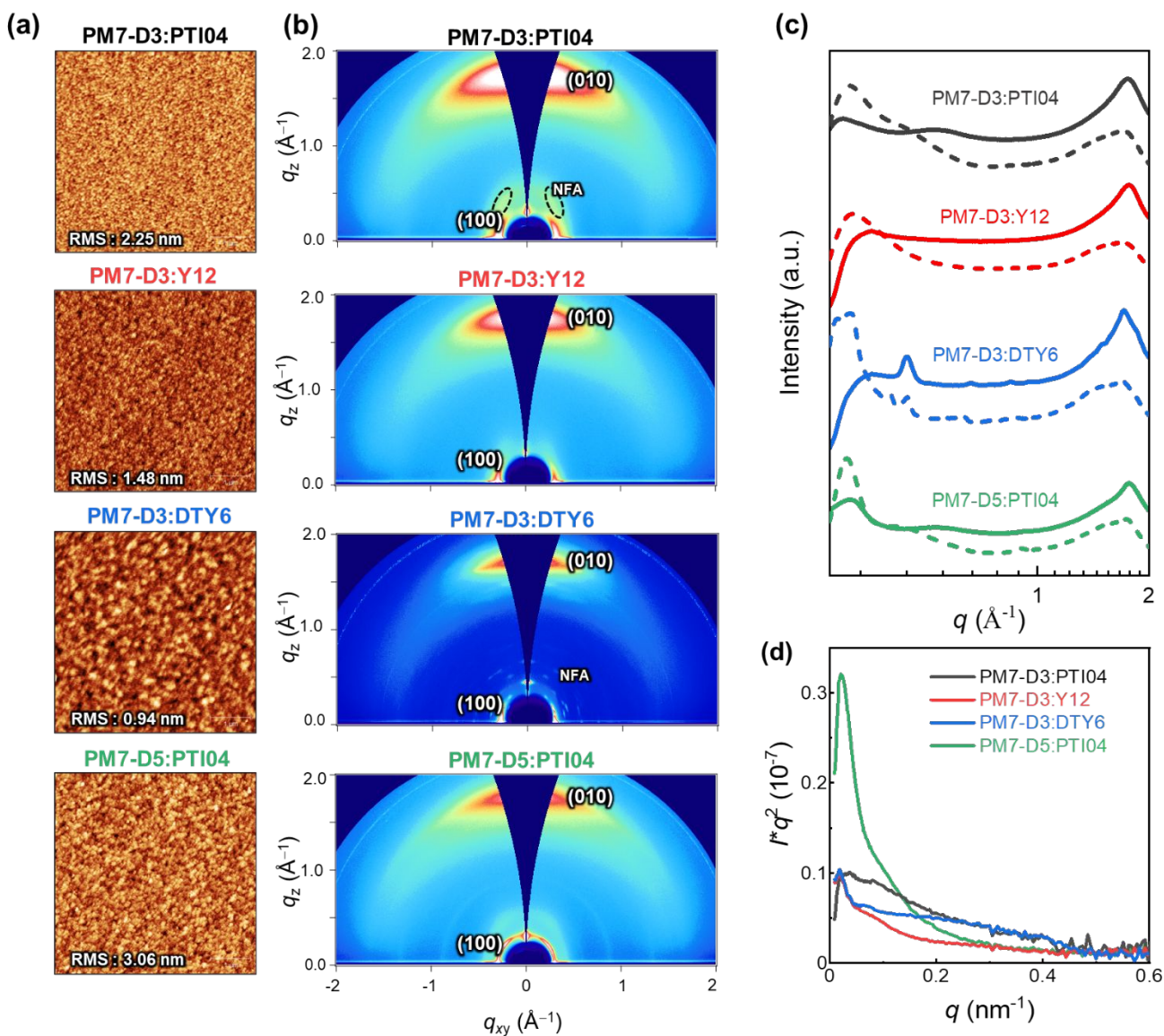
4 **Table 2.** Summary of the device parameters obtained under simulated AM1.5G illumination.

D:A	ξ	$N_{t,bulk}$ (cm^{-3})	$N_{t,surf}$ (cm^{-3})	$\tau\mu$ ($\text{cm}^2 \text{V}^{-1}$)	L_{dr} (nm)	$L_{dr/d}$	L_{diff} (nm)	$L_{diff/d}$
PM7-D3:PTI04	0.035	1.16E+12	6.97E+12	1.17E-09	1044.03	10.44	54.77	0.55
PM7-D3:Y12	0.021	1.56E+13	1.63E+14	8.83E-10	742.37	7.35	47.62	0.47
PM7-D3:DTY6	0.027	7.55E+14	6.68E+13	7.54E-10	661.77	6.75	44.02	0.45
PM7-D5:PTI04	0.028	4.02E+13	1.66E+13	6.64E-10	600.11	6.00	41.30	0.41

5
 6 To obtain quantitative insights into the charge recombination dynamics, we employ a model
 7 that relates the recombination current density J_{rec} to the charge carrier density and compares it to
 8 experimental values of J_{rec} obtained from J - V curves, which can be achieved by a combination of
 9 J - V characteristics (in the dark and under illumination) and voltage-dependent impedance
 10 analysis.^{42, 45} The density of bulk traps $N_{t,bulk}$, the density of surface traps $N_{t,surf}$, and the reduction
 11 factor (also known as Langevin prefactor) ξ are parameters used to fit the recombination current
 12 with the experimental data.⁵⁶ A summary of the physical parameters used in the J_{rec} fitting model
 13 is presented in **Table 2**. Even though it shows a slightly higher Langevin prefactor correlating to
 14 bimolecular recombination due to its higher μ_{eff} , it is worth noting that both bulk and surface trap
 15 density dramatically decrease in PM7-D3:PTI04 system, suppressing charge carrier loss due to
 16 bulk and surface trap-assisted recombination in the device. Also, benefiting from the high mobility,
 17 the calculated $\tau\mu$ for the PM7-D3:PTI04 device exhibits the smallest value among the four systems,

1 a feature that has been shown to correlate with a high FF in earlier reports.^{57, 58} Next, the drift
2 length (L_{dr}) and diffusion length (L_{diff}) in the BHJ active layers are calculated based on $n(V)$ and
3 μ_{eff} , which are further normalized by the thickness of the film. Considering the relatively long L_{dr}
4 (all above 600 nm) compared with the average thickness of the active layers (~ 100 nm), longer
5 L_{diff} in the PM7-D3:PTI04 system makes a difference when the internal electric field is small. In
6 other words, the drift length at J_{sc} is much greater than the thickness of the active layer. However,
7 the effective diffusion length is smaller than the active layer thickness, which can result in
8 significant losses in carrier extraction when drift is not efficient.⁵⁸ The charge transport and
9 collection processes are mainly controlled by the diffusion process and benefit from the long L_{diff}
10 in the PM7-D3:PTI04 system when getting close to maximum power voltage (V_{mp}) and V_{oc}
11 conditions, which ultimately explains the higher PCE of the PM7-D3:PTI04 solar cells among the
12 four blend systems. Key takeaway from the detailed analysis of photovoltaic parameters is that the
13 PM7-D3:PTI04 system has lower surface- and bulk-trap assisted recombination and efficient
14 charge extraction and collection resulting in a high FF and J_{sc} . Meanwhile, the lowest bulk traps
15 in PM7-D3:PTI04 system also suppress the non-radiative voltage loss and lead to a high V_{oc} . In
16 contrast, the other PM7-D3:MA blends suffer from relatively high recombination rates and low
17 FF , leading to poor performance in the OPV devices. The presence of significant bulk traps within
18 the PM7-D3:DTY6 system results in serious non-radiative voltage losses, leading to a limitation
19 in its V_{oc} and overall device performance. The PM7-D5:PTI04 devices also suffer from these
20 factors, indicating that both donor and acceptor molecules and their packing interactions are
21 particularly important in order to steer the electronic properties of the BHJ blends toward high
22 PCE values. This led us to investigate the BHJ morphology and molecular origins of the different
23 photovoltaic properties, as discussed below.

1 2.3. Resolving BHJ morphology at different length scales



2
3 **Figure 3.** Surface and bulk morphology of the BHJ blends processed from 2-MeTHF: (a) AFM
4 topography images $5 \mu\text{m} \times 5 \mu\text{m}$, (b) 2D GIWAXS patterns, (c) the corresponding log-log plot
5 of in-plane (dash lines) and out-of-plane (solid lines) GIWAXS profiles, and (d) RSoXS
6 profiles at 285.0 eV with film thickness normalization and Lorentz correction.

1 The charge generation, transport, recombination, and extraction processes in OPVs are closely
2 linked to the BHJ morphology and packing arrangements of the donor-acceptor moieties.^{43, 59-62} In
3 particular, the processing solvent has a significant impact on the BHJ morphology.⁶³⁻⁶⁵ To gain
4 further insights into the impact of the sidechain positions and lengths on the device performance
5 of the four OPV systems processed from 2-MeTHF, the BHJ morphologies were further
6 characterized with various techniques at different length scales (μm to sub-nm).⁶⁶ At the micron
7 to sub-micron length scales, AFM is employed to map the topography of PM7-D3:PTI04, PM7-
8 D3:Y12, PM7-D3:DTY6, and PM7-D5:PTI04 blends under optimized conditions. As shown in
9 **Figure 3a**, AFM images of all BHJ blends at $5 \mu\text{m} \times 5 \mu\text{m}$ reveal continuous networks and
10 relatively smooth surfaces with RMS values from $\sim 1 \text{ nm}$ - 3.06 nm .

11 GIWAXS measurements were conducted to gain insights into the molecular packing and
12 orientation of the D and A molecules with respect to the substrate. The two-dimensional (2D)
13 patterns of all blend films exhibit a combination of features from the donor polymers (PM7-D3
14 and PM7-D5) and MAs, as illustrated in **Figure 3b**. The GIWAXS data for neat donor and acceptor
15 are shown in Figure S16. All the PM7-D3 systems displayed distinct (010) scattering patterns in
16 the out-of-plane direction originating from the π - π stacking of the polymer donor and MAs, which
17 indicates a preferred face-on orientation in an ordered structure. A comprehensive summary of all
18 relevant parameters and details can be found in the SI, Table S5.

19 All blends exhibit a moderate coherence length ($C_L = 10\text{-}20 \text{ nm}$) for (100) scattering, which
20 corresponds to length scale over which the sample scatter coherently and indicates the quality of
21 the molecular packing. It is comparable to the exciton diffusion lengths in oligo-/polymeric organic
22 semiconductors.^{67, 68} Importantly, the molecular packing of PTI04 remained intact, as evidenced
23 by the side scattering feature observed at $q_z = 0.36 \text{ \AA}^{-1}$, which corresponds to the characteristic

1 scattering of neat PTI04. This observation suggests that the incorporation of PM7-D3 and PTI04
2 into the blend film does not disrupt the formation of their respective molecular packing during the
3 blending process. In contrast, in the case of PM7-D3:Y12 system, although it exhibits a preferred
4 face-on orientation indicative of ordered structures, the scattering feature corresponding to neat
5 Y12 is undetected. This disruption of molecular packing upon mixing is consistent with the results
6 obtained from ss-NMR measurements to be discussed. While the increased volume fraction of
7 MAs in D:A domains can potentially enhance J_{sc} by facilitating efficient charge generation, it can
8 also lead to a higher probability of recombination events, thereby adversely affecting the FF . These
9 findings align well with the observed photovoltaic properties of the PM7-D3:Y12 system, which
10 exhibits high J_{sc} values but low FF . Unlike the Y12 system, the PM7-D3:DTY6 system exhibits
11 completely different behavior. In this case, the scattering feature originating from the DTY6 crystal
12 remains in the blend. This intense scattering can be attributed to the poor miscibility between the
13 donor and acceptor components supported by the value of the Flory-Huggins parameter, which
14 will be further discussed below. While an improved molecular order of the acceptor component
15 can enhance electron transport, an excessive presence of acceptor crystallites can have a
16 detrimental effect on charge transport since the acceptor crystallite islands may work as traps.
17 These findings provide an explanation for the observed high FF but low J_{sc} of the PM7-D3:DTY6
18 system. When PM7-D3 is replaced with PM7-D5, no significant changes are observed in the 2D
19 GIWAXS analysis of PM7-D5:PTI04.

20 To gain detailed information on the amorphous mixed phases, RSoXS measurements were
21 conducted on all four studied systems.^{69, 70} Details of long period estimation by RSoXS
22 measurements and analyses are presented in SI, Table S6. These results suggest that all four blend
23 films exhibit multi-length scale morphology with larger domains with a long period of ~120 - 220

1 nm and smaller domains with a long period of ~15 - 30 nm. The PM7-D3:PTI04 system contains
2 the highest volume fraction (69%) of the smaller domains with an average size of 26 nm. For the
3 other three systems, the volume fractions and long periods of the smaller domains are: PM7-
4 D3:Y12 (63%, 51 nm), PM7-D3:PTI04 (56%, 17 nm), and PM7-D5:PTI04 (26%, 29 nm).
5 Previously, strong correlations between FF and scattering intensity/domain purity have been
6 observed in both single-mode and multi-mode morphologies, particularly if such morphologies
7 were for the same material system and processing was varied.⁷¹⁻⁷³ Similarly, domains size could
8 be often correlated to J_{sc} .⁷⁴ Using morphological parameters to explain relative device performance
9 is more difficult and complex if devices are compared using different materials systems, as device
10 performance depends on many parameters and materials' intrinsic properties such as charge
11 generation, charge carrier mobility, and recombination.⁷⁵ Reasonable rough correlations between
12 morphology and performance are observed here. For example, the high J_{sc} of PM7-D3:PTI04
13 blends agrees with the large volume fraction of small domains. However, no clear self-consistent,
14 *i.e.* monotonic trend in FF or J_{sc} with a range of morphological parameters can be observed across
15 all four material systems. This indicates that other parameters such as intrinsic mobilities of the
16 materials, energetic offsets at interfaces, differences in interfacial structure, or vertical gradients
17 make a significant contribution to the relative device performance.

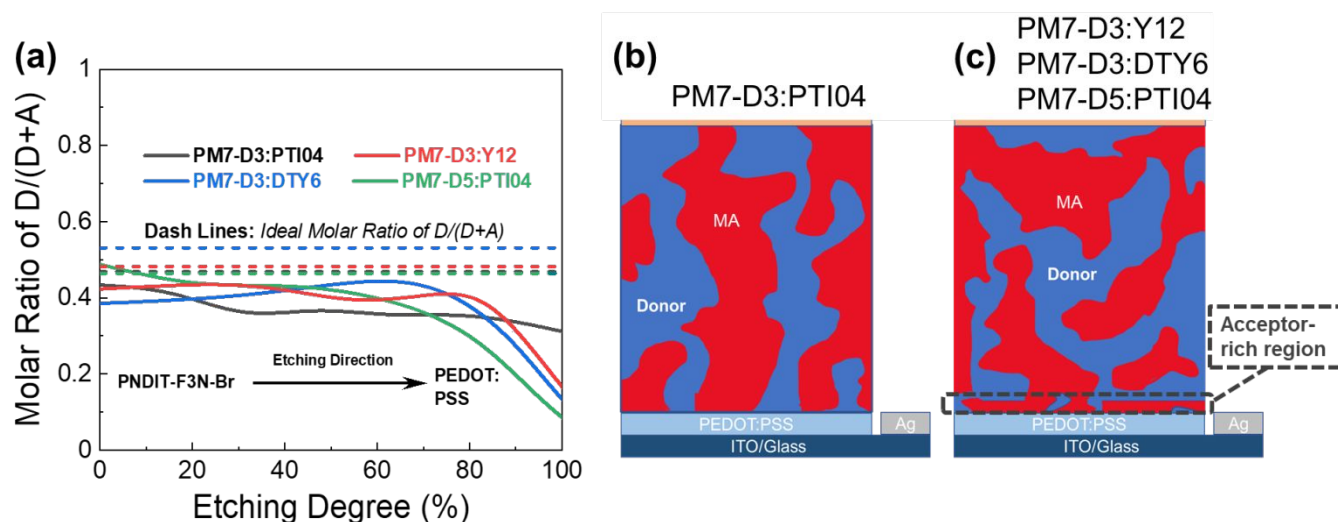


Figure 4. (a) XPS depth profile of PM7-D3:PTI04, PM7-D3:Y12, PM7-D3:DTY6, and PM7-D5:PTI04 BHJ films showing D/(A+D) molar ratio evolution as a function of etching degree, where etching begins at the top air/film interface. Dotted lines represent the ideal D/(D+A) molar ratio calculated from the original D:A ratio of 1:1.2 by weight. (b) Schematics of the PM7-D3:PTI04 blend with more uniform vertical phase separation and (c) of the other three blend films showing vertical phase gradation with an acceptor-rich region near the blend/PEDOT:PSS interface.

The BHJ films were also characterized using depth-profiled X-ray photoelectron spectroscopy (XPS) to investigate the impact of sidechain length and position on the donor and acceptor distribution and composition in the vertical direction of the active layers.⁷⁶ The distribution of the PM7-series donors and Y-series MAs can be tracked by the chlorine (Cl) signal and fluorine (F) signal, respectively, considering the fact that F is absent in the donors and Cl is absent in the acceptors. As a result of the different active layer thicknesses, the etching time to reach the bottom of the active layer is slightly different among the blends. The ratio of D/(D+A) for each blend was calculated from the representative elemental ratio of the polymers and MAs (**Figure 4**). As shown

1 in **Figure 4a**, an overall decrease in the $D/(A+D)$ molar ratio is observed in the vertical phase
2 separation for all the blend films. In all cases, the donor polymers accumulate more at the top
3 blend/air interface, while a molecular acceptor-enriched region can be observed close to the bottom
4 of the BHJ layer, yet different trends in the depth profile are observed for the BHJ blends with
5 different acceptors. In particular, the PM7-D3:PTI04 blend tends to be more uniform in the vertical
6 phase arrangement with a gradual reduction of the $D/(A+D)$ ratio from 0.43 to 0.31 upon going
7 from top to bottom. In the other three blends, a dramatic drop of the donor component occurs after
8 reaching 70% etching, and a region of ~ 10 nm is dominated by MA molecules at the bottom of the
9 active layers. These are illustrated by two different schematic diagrams (**Figures 4b** and **4c**)
10 showing the vertical gradation trends in the microstructure of the PM7-D3:PTI04 blend and the
11 other three systems. A significant number of acceptors accumulated at the bottom of the BHJ layer
12 can have a negative impact on the device performance of the PM7-D3:Y12, PM7-D3:DTY6, and
13 PM7-D5:PTI04 systems. Undesirable surface-trap-assisted recombination can occur as a result of
14 the enrichment in acceptors at the interface between the PEDOT:PSS layer and the active layer.
15 Compared with these blends, a uniform distribution in the vertical phase of the PM7-D3:PTI04
16 film implies higher miscibility of PM7-D3:PTI04 blend with PEDOT:PSS layer, which can
17 contribute to reducing the density of traps and suppressing the trap-assisted recombination of
18 charge carriers in the OPV device, especially surface-trap-assisted recombination, and thus lead to
19 a more efficient charge collection process.⁷⁶ The miscibility between PM7-D3 and PTI04 could be
20 further investigated by the Flory–Huggins interaction parameter χ_{F-H} derived from the contact
21 angle measurements (CAM) (SI, Table S7). The polar and dispersive surface tension of the
22 measured films can be derived based on the CAM obtained by using water and glycerol as specific
23 solvents, which describes the solubility parameters of the studied donor and MAs. And χ_{F-H} can be

1 calculated by comparing the difference of solubility parameters between different donor and
2 acceptor materials. Typically, the better the miscibility between two studied materials, the smaller
3 the value of χ_{F-H} .^{77, 78} Among all four studied D:A blends, PM7-D3:PTI04 shows the smallest χ_{F-H}
4 value of 0.036 as compared to the other three blends (0.233 for PM7-D3:Y12, 2.089 for PM7-
5 D3:DTY6, and 0.177 for PM7-D5:PTI04). The lower χ value found for PM7-D3:PTI04 further
6 confirms the better miscibility of D:A in the active layer. These results are not only consistent with
7 the higher D:A interfacial areas from the RSoXS measurement, but also with the effective mobility
8 and the recombination current fitting analysis discussed in the device physics part, which further
9 confirms the origin of the surface trap in the studied systems. A favorable vertical gradient of the
10 active layer increases the probability of excitons reaching and dissociating at the polymer and MA
11 interfaces, promoting higher effective mobility ($\mu_{\text{eff}} \sim 10^{-4} \text{ cm}^2 \text{ V}^{-1} \text{ s}^{-1}$), lower trap density (both
12 in the bulk and at the surface), and lower non-radiative recombination loss in the PM7-D3:PTI04
13 system compared with the others, which is consistent with the higher observed PCE.

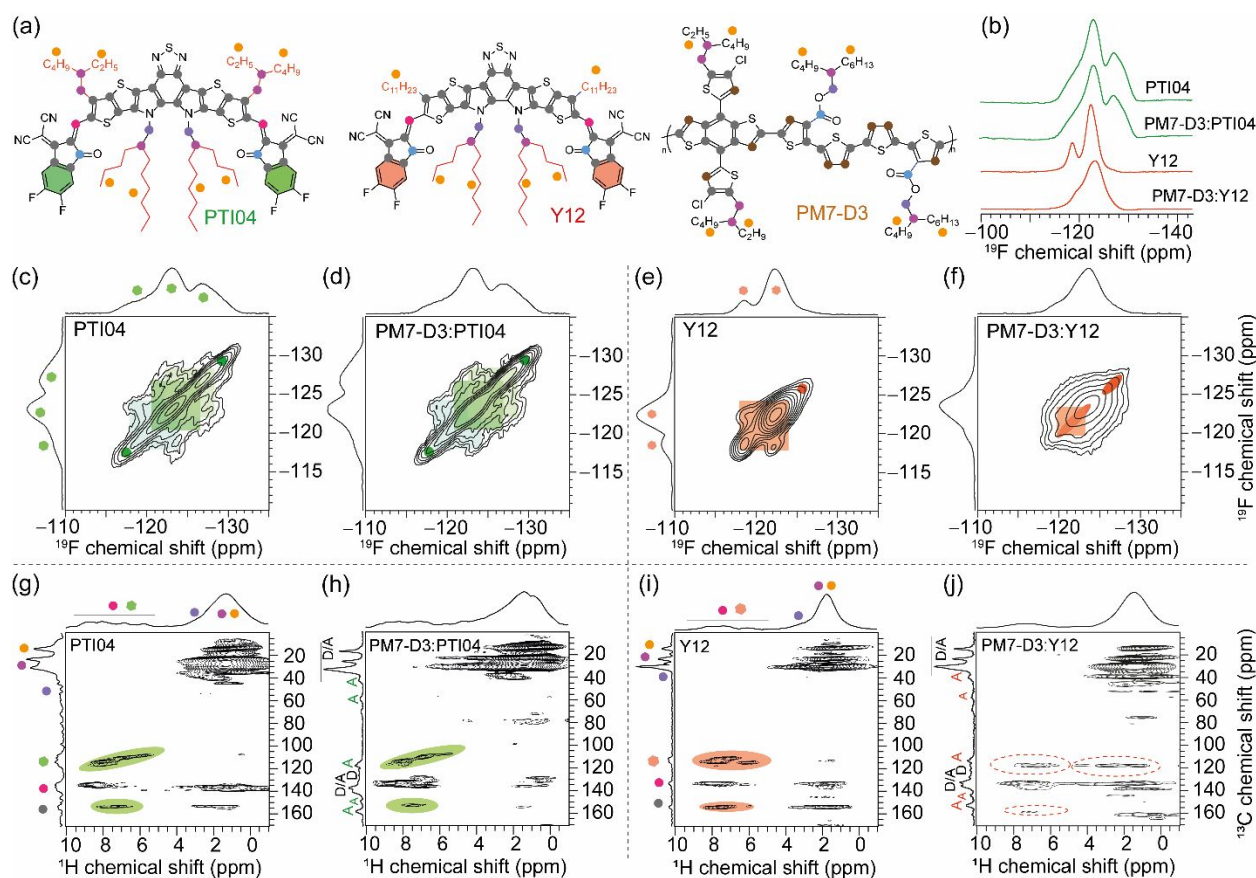
14 Within the resolution capabilities of the above techniques, the analysis of long-range order at
15 the surface, bulk, and interfacial BHJ morphology indicates that the acceptor domains exhibit
16 different morphological features as observed by means of lamellar stacking peaks of blend films
17 in GIWAXS plots and the XPS depth profile analysis. However, these data and observations do
18 not resolve the molecular origins of the different acceptor morphology induced by the PTI04,
19 DTY6, and Y12 molecules in the PM7-D3:MA BHJ blend films. In other words, changes in the
20 bulk and interfacial morphology of Y12 and PTI04 molecules are expected to contribute to
21 different performances in OPV devices. The local chemical environments of end groups and
22 sidechains in acceptor morphology are known to be sensitive to solvent processing, which can be

1 only identified and distinguished by gaining access to atomic-level resolution enabled by ssNMR
2 spectroscopy as discussed below.⁶³

3 **2.4. Local structures and intermolecular interactions**

4 Molecular-level origins of the different local structures and packing interactions in neat
5 materials and blends can be characterized by ssNMR spectroscopy.^{42, 63, 79-83} To resolve the
6 different packing interactions in acceptor morphology that contribute to the different PCE values
7 in OPV devices, we have selected the PM7-D3:PTI04 and PM7-D3:Y12 blends, owing to the
8 differences in their PCE values (**Table 1**). For the neat PM7-D3, PTI04, and Y12 compounds and
9 the BHJ blends, the short-range order and intermolecular interactions are examined by analyzing
10 the ¹H, ¹³C, and ¹⁹F chemical shifts (**Figure 5**, and SI, Figures S18-S19) and through-space dipole-
11 dipole interactions between them. The local chemical environment of the ¹⁹F species in the 2-(5,6-
12 difluoro-3-oxo-2,3-dihydro-1H-inden-1-ylidene)malononitrile (2FIC) terminal groups (henceforth
13 referred to as *end groups*) in the PTI04 and Y12 molecules lead to different ¹⁹F chemical shifts;^{4,}
14 ⁶⁶ it is observed that PTI04 retains its local morphology in the BHJ blend but the Y12 molecules
15 do not. The different ¹⁹F peaks are due to the different intermolecular interactions between the end
16 groups and the sidechains and the fused ring core, as previously observed for Y-series molecules.⁶³
17 Two-dimensional (2D) ¹⁹F-¹⁹F, ¹H-¹³C and ¹H-¹H correlation NMR spectroscopy measurements
18 further corroborate these results (**Figure 5** and Figure S18; a detailed discussion of peak analysis
19 is presented in SI). The local morphology of PTI04 is retained in the BHJ blend, likely due to the
20 strong inter- and intramolecular interactions between the end-groups and sidechains of PTI04
21 (green color ovals in **Figures 5c,d,g,h**). In contrast, subtle structural changes in the vicinity of end
22 groups and sidechains are observed in Y12 molecules and the PM7-D3:Y12 BHJ blend leading to

1 different chemical shifts and peak intensities, as highlighted by the red color ovals in **Figures**
 2 **5e,f,i,j**.



3
 4 **Figure 5.** (a) Structures of PM7-D3, PTI04, and Y12 with color dots to guide the analysis of
 5 2D NMR spectra. (b) Solid-state 1D ^{19}F MAS NMR spectra of MAs and PM7-D3:MA blends.
 6 Solid-state 2D ^{19}F - ^{19}F spin-diffusion NMR spectra of (c) neat PTI04 and (d) PM7-D3:PTI04
 7 indicating the identical acceptor morphology, and (e) neat Y12 and (f) PM7-D3:Y12 blend
 8 films with different peak patterns highlighted in red. Solid-state 2D ^1H - ^{13}C HETCOR NMR
 9 spectra of (g) neat PTI04 and (h) PM7-D3:PTI04 indicating the identical local acceptor
 10 morphology as depicted by green ovals, and (i) neat Y12 and (j) PM7-D3:Y12 BHJ blend films
 11 showing the difference in the local morphology as depicted in the red dashed ovals.

12

1 Further insights into the local morphology and structural aspects of PM7-D3 moieties and MAs
2 in neat compounds and in the BHJ blends are obtained by analyzing 2D ^1H - ^1H double-quantum –
3 single-quantum (DQ-SQ) spectra (SI, Figure S20). The most notable aspect is that the changes in
4 the inter- and intramolecular interactions among end-groups/sidechains in Y12 lead to the different
5 2D ^1H - ^{13}C peaks. Therefore, local morphology changes around the Y12 molecules in the vicinity
6 of the end groups as well as the branched sidechains (depicted in ovals), are expected to contribute
7 to the performance deterioration in the PM7-D3:Y12-based OPVs. These observations are
8 consistent with the AFM, GIWAXS, and XPS data that showed different surface and bulk
9 morphologies with different lamellar packing distances and domain sizes of the D-A moieties in
10 the 2-MeTHF processed BHJ blends, which impacts the charge generation, transport and
11 extraction processes.

12 **3. Conclusions**

13 In summary, the green solvent processed PM7-D3:PTI04 device exhibit a PCE approaching 15%,
14 comparable to the well-known PM6:Y6 system processed from traditional halogenated solvents
15 and additives. In understanding the structure-processing-property relationships, the key learnings
16 obtained from the device physics data and characterization at different length scales ranging from
17 microns to sub-nanometer distances can be summarized as follows:

- 18 1. The enhanced solubility of PM7-D3 polymer in 2-MeTHF due to its more flexible
19 backbone structure leads to a better mixing and more optimal phase separation in the
20 PM7-D3:PTI04 BHJ morphology. This results in enhanced J - V characteristics and FF
21 and reduced bulk and surface trap-assisted recombinations. These factors combine to
22 produce a high PCE value of 14.9% in the OPV devices. In contrast, the less favorable
23 BHJ morphology in the other blends with MAs such as DTY6 and Y12, as well as

- 1 PM7-D5:MA blends, leads to higher trap-assisted recombination dynamics and
2 reduced performance in the OPV devices.
- 3 2. The surface and bulk BHJ morphologies consisting of favorable D/A separation and
4 domain purity are paramount for the high efficiency achieved in the PM7-D3:PTI04
5 based OPV devices processed from 2-MeTHF solvent, as revealed by the AFM, 2D
6 GIWAXS, and RSoXS data. The high-performance PTI04-based systems exhibit
7 domain sizes of ~26 nm vs. much larger domains for the other MAs in the BHJ blends.
- 8 3. At a few tens of nm scale, the long-range order associated with π - π stacked and
9 lamellae stacked D and A moieties in the out-of-the-plane direction with respect to the
10 substrates is expected to be beneficial for charge transport in all devices, although
11 significant disruption in such interactions in PM7-D3:Y12 leads to its poorer
12 efficiency.
- 13 4. The compositional and spatial distributions of the D and A domains in the vertical
14 direction are important for charge generation and extraction. The PM7-D3:PTI04
15 systems exhibit favorable morphology while the PM7-D3:Y12 BHJ blend shows Y12
16 molecules phase-separated into larger domains at the photoactive/PEDOT:PSS
17 interfaces, leading to higher charge recombination and therefore low *FF*.
- 18 5. Examining the local packing interactions at sub-nanometer distances, the
19 backbone/sidechain interactions stabilize the donor and MAs morphology. The length
20 of the branched sidechains attached to the core in PTI04 is particularly important in
21 maintaining the self-assembly and phase separation in the BHJ morphology, as
22 revealed by ssNMR.⁶³

1 6. Overall, the molecular design associated with the donor polymers and MAs in this
2 study including the core and sidechain engineering has a significant impact on the
3 solubility, processability, morphology, and charge carrier properties of the 2-MeTHF
4 processed OPV devices. A preferred average domain size of ~25 nm with relatively
5 high domain purity and more uniform distribution of D and A inter-mixing is observed
6 in the PM7-D3:PTI04 BHJ film compared to the other D:A blends, which facilitates
7 the charge generation and collection processes while limiting the trap-assisted
8 recombination process in the device, leading to highly effective mobility and
9 remarkable performance.

10

11 Thus, this work provides insight into the structure-morphology-property relationships essential for
12 developing environmentally friendly and commercially viable high-performance OPVs.

13

14 **Conflicts of interest**

15 There are no conflicts of interest to declare

16

17 **Acknowledgments**

18 Z. D. and Z. Z. acknowledge funding from the Air Force Office of Scientific Research (AFOSR)
19 Grant #FA9550-19-1-0348.

20 D. C., S. C. and T.-Q. N. thank the Office of Naval Research (ONR) Grant #N00014-21-1-2181
21 through the Multidisciplinary University Research Initiative program.

22 S. S., A. L. J., and J. R. R. acknowledge the Office of Naval Research (ONR) Grant #N00014-
23 21-1-2144 through the Multidisciplinary University Research Initiative program.

1 P. T., J. Z. and S. R. M. acknowledge the Department of the Navy, Office of Naval Research
2 Multidisciplinary University Research Initiative Award #N00014-20-1-2167, and #N00014-21-1-
3 2180. P. T. acknowledges the support from Vidyasirimedhi Institute of Science and Technology
4 (VISTEC).

5 Z. P. and H. A. acknowledge the support from the U.S. Office of Naval Research Grant #N00014-
6 20-1-2155. RSoXS data were acquired at beamlines 11.0.1.2 at the Advanced Light Source, LBNL,
7 which is supported by the Director of the Office of Science, Office of Basic Energy Sciences, of
8 the U.S. Department of Energy under Contract No. DE-AC02-05CH11231.

9 C. W. and G. N. M. R. gratefully acknowledge the financial support from University of Lille, EU
10 H2020 (grant no. 795091) and INFRANALYTICS FR 2040 for carrying out experiments at high
11 field NMR facility at Lille.

12 The work at the University of Arizona has been supported by the Office of Naval Research under
13 Awards #N00014-21-1-2182 through the Multidisciplinary University Research Initiative program
14 and #N00014-20-1-2110.

15 The authors gratefully thank Dr. Joachim Vollbrecht, Dr. Tom Mates, and Dr. Oleksandr Polonskyi
16 for useful discussions.

17

References

1. A. J. Heeger, *Adv. Mater.*, 2014, **26**, 10-28.
2. J. Hou, O. Inganäs, R. H. Friend and F. Gao, *Nature materials*, 2018, **17**, 119-128.
3. S. Albrecht, J. R. Tumbleston, S. Janietz, I. Dumsch, S. Allard, U. Scherf, H. Ade and D. Neher, *J. Phys. Chem. Lett.*, 2014, **5**, 1131-1138.
4. A. Karki, J. Vollbrecht, A. J. Gillett, S. S. Xiao, Y. L. Yang, Z. X. Peng, N. Schopp, A. L. Dixon, S. Yoon, M. Schrock, H. Ade, G. N. M. Reddy, R. H. Friend and T. Q. Nguyen, *Energy & Environmental Science*, 2020, **13**, 3679-3692.
5. Y. Cui, Y. Xu, H. Yao, P. Bi, L. Hong, J. Zhang, Y. Zu, T. Zhang, J. Qin, J. Ren, Z. Chen, C. He, X. Hao, Z. Wei and J. Hou, *Adv. Mater.*, 2021, **33**, e2102420.
6. L. Zhu, M. Zhang, J. Xu, C. Li, J. Yan, G. Zhou, W. Zhong, T. Hao, J. Song, X. Xue, Z. Zhou, R. Zeng, H. Zhu, C. C. Chen, R. C. I. MacKenzie, Y. Zou, J. Nelson, Y. Zhang, Y. Sun and F. Liu, *Nat Mater*, 2022, **21**, 656-663.
7. S. Zhang, L. Ye, H. Zhang and J. Hou, *Materials Today*, 2016, **19**, 533-543.
8. D. Corzo, D. Rosas-Villalva, G. Tostado-Blázquez, E. B. Alexandre, L. H. Hernandez, J. Han, H. Xu, M. Babics, S. De Wolf and D. Baran, *Nature Energy*, 2023, **8**, 62-73.
9. M. Ghasemi, N. Balar, Z. Peng, H. Hu, Y. Qin, T. Kim, J. J. Rech, M. Bidwell, W. Mask, I. McCulloch, W. You, A. Amassian, C. Risko, B. T. O'Connor and H. Ade, *Nature Materials*, 2021, **20**, 525-532.
10. I. Burgués-Ceballos, F. Machui, J. Min, T. Ameri, M. M. Voigt, Y. N. Luponosov, S. A. Ponomarenko, P. D. Lacharmoise, M. Campoy-Quiles and C. J. Brabec, *Advanced Functional Materials*, 2014, **24**, 1449-1457.
11. D. T. Duong, B. Walker, J. Lin, C. Kim, J. Love, B. Purushothaman, J. E. Anthony and T. Q. Nguyen, *Journal of Polymer Science Part B: Polymer Physics*, 2012, **50**, 1405-1413.
12. B. Walker, A. Tamayo, D. T. Duong, X. D. Dang, C. Kim, J. Granstrom and T. Q. Nguyen, *Advanced Energy Materials*, 2011, **1**, 221-229.
13. Q. He, W. Sheng, M. Zhang, G. Xu, P. Zhu, H. Zhang, Z. Yao, F. Gao, F. Liu, X. Liao and Y. Chen, *Advanced Energy Materials*, 2021, **11**, 2003390.
14. H. Zhang, Y. Li, X. Zhang, Y. Zhang and H. Zhou, *Materials Chemistry Frontiers*, 2020, **4**, 2863-2880.
15. K. S. Wienhold, V. Körstgens, S. Grott, X. Jiang, M. Schwartzkopf, S. V. Roth and P. Müller-Buschbaum, *ACS Applied Materials & Interfaces*, 2019, **11**, 42313-42321.
16. Z. Zheng, E. He, J. Wang, Z. Qin, T. Niu, F. Guo, S. Gao, Z. Ma, L. Zhao, X. Lu, Q. Xue, Y. Cao, G. T. Mola and Y. Zhang, *Journal of Materials Chemistry A*, 2021, **9**, 26105-26112.
17. J. Peet, J. Y. Kim, N. E. Coates, W. L. Ma, D. Moses, A. J. Heeger and G. C. Bazan, *Nature materials*, 2007, **6**, 497-500.
18. C. V. Hoven, X. D. Dang, R. C. Coffin, J. Peet, T. Q. Nguyen and G. C. Bazan, *Adv. Mater.*, 2010, **22**, E63-E66.
19. J. T. Rogers, K. Schmidt, M. F. Toney, G. C. Bazan and E. J. Kramer, *Journal of the American Chemical Society*, 2012, **134**, 2884-2887.
20. L. A. Perez, K. W. Chou, J. A. Love, T. S. Van Der Poll, D. M. Smilgies, T. Q. Nguyen, E. J. Kramer, A. Amassian and G. C. Bazan, *Adv. Mater.*, 2013, **25**, 6380-6384.
21. C. McDowell, M. Abdelsamie, M. F. Toney and G. C. Bazan, *Adv. Mater.*, 2018, **30**, 1707114.

- 1 22. H. Gaspar, G. Bernardo and A. Mendes, *Nanoenergy Advances*, 2021, **2**, 1-28.
- 2 23. H. Yu, S. Luo, R. Sun, I. Angunawela, Z. Qi, Z. Peng, W. Zhou, H. Han, R. Wei, M. Pan,
3 A. M. H. Cheung, D. Zhao, J. Zhang, H. Ade, J. Min and H. Yan, *Advanced Functional*
4 *Materials*, 2021, **31**, 2100791.
- 5 24. Z. Du, M. Mainville, J. Vollbrecht, A. L. Dixon, N. Schopp, M. Schrock, Z. Peng, J.
6 Huang, S. Chae, H. Ade, M. Leclerc, G. N. M. Reddy and T.-Q. Nguyen, *Solar RRL*,
7 2021, **5**, 2100213.
- 8 25. S. Dong, T. Jia, K. Zhang, J. Jing and F. Huang, *Joule*, 2020, **4**, 2004-2016.
- 9 26. D. Wang, G. Zhou, Y. Li, K. Yan, L. Zhan, H. Zhu, X. Lu, H. Chen and C.-Z. Li,
10 *Advanced Functional Materials*, 2022, **32**, 2107827.
- 11 27. S. Zhang, H. Chen, P. Wang, S. Li, Z. Li, Y. Huang, J. Liu, Z. Yao, C. Li, X. Wan and Y.
12 Chen, *Solar RRL*, 2023, **7**, 2300029.
- 13 28. Z. Chen, L. Yan, J. J. Rech, J. Hu, Q. Zhang and W. You, *ACS Applied Polymer*
14 *Materials*, 2019, **1**, 804-814.
- 15 29. H. Huang, X. J. Li, C. K. Sun, I. Angunawela, B. B. Qiu, J. Q. Du, S. C. Qin, L. Meng, Z.
16 J. Zhang, H. Ade and Y. F. Li, *Journal of Materials Chemistry C*, 2020, **8**, 7718-7724.
- 17 30. V. Pace, P. Hoyos, L. Castoldi, P. Domínguez de María and A. R. Alcántara,
18 *ChemSusChem*, 2012, **5**, 1369-1379.
- 19 31. O. Al Musaimi, Y. E. Jad, A. Kumar, A. El-Faham, J. M. Collins, A. Basso, B. G. de la
20 Torre and F. Albericio, *Organic Process Research & Development*, 2018, **22**, 1809-1816.
- 21 32. L. Hong, H. Yao, Z. Wu, Y. Cui, T. Zhang, Y. Xu, R. Yu, Q. Liao, B. Gao and K. Xian,
22 *Adv. Mater.*, 2019, **31**, 1903441.
- 23 33. Z. Li, L. Ying, P. Zhu, W. Zhong, N. Li, F. Liu, F. Huang and Y. Cao, *Energy &*
24 *Environmental Science*, 2019, **12**, 157-163.
- 25 34. L. Bucher, L. Tanguy, N. Desbois, P. L. Karsenti, P. D. Harvey, C. P. Gros and G. D.
26 Sharma, *Solar RRL*, 2018, **2**, 1700168.
- 27 35. J. Panidi, E. Mazzolini, F. Eisner, Y. Fu, F. Furlan, Z. R. Qiao, M. Rimmele, Z. Li, X. H.
28 Lu, J. Nelson, J. R. Durrant, M. Heeney and N. Gasparini, *Acs Energy Letters*, 2023, **8**,
29 3038-3047.
- 30 36. X. Chen, X. Liu, M. A. Burgers, Y. Huang and G. C. Bazan, *Angewandte Chemie*
31 *International Edition*, 2014, **53**, 14378-14381.
- 32 37. S. V. Dayneko, A. D. Hendsbee and G. C. Welch, *Chemical Communications*, 2017, **53**,
33 1164-1167.
- 34 38. C. Liao, M. Zhang, X. Xu, F. Liu, Y. Li and Q. Peng, *Journal of Materials Chemistry A*,
35 2019, **7**, 716-726.
- 36 39. J. Yuan, Y. Zhang, L. Zhou, G. Zhang, H.-L. Yip, T.-K. Lau, X. Lu, C. Zhu, H. Peng, P.
37 A. Johnson, M. Leclerc, Y. Cao, J. Ulanski, Y. Li and Y. Zou, *Joule*, 2019, **3**, 1140-1151.
- 38 40. I. Pelse, A. L. Jones, L. J. Richter and J. R. Reynolds, *Chemistry of Materials*, 2021, **33**,
39 657-667.
- 40 41. F. C. Spano and C. Silva, *Annual review of physical chemistry*, 2014, **65**, 477-500.
- 41 42. Z. Du, M. Mainville, J. Vollbrecht, A. L. Dixon, N. Schopp, M. Schrock, Z. Peng, J.
42 Huang, S. Chae, H. Ade, M. Leclerc, G. N. M. Reddy and T.-Q. Nguyen, *Solar RRL*,
43 2021, **5**, 2100213.
- 44 43. H.-C. Liao, C.-C. Ho, C.-Y. Chang, M.-H. Jao, S. B. Darling and W.-F. Su, *Materials*
45 *today*, 2013, **16**, 326-336.

- 1 44. N. Gasparini, A. Gregori, M. Salvador, M. Biele, A. Wadsworth, S. Tedde, D. Baran, I.
2 McCulloch and C. J. Brabec, *Advanced Materials Technologies*, 2018, **3**, 1800104.
- 3 45. J. Vollbrecht, V. V. Brus, S. J. Ko, J. Lee, A. Karki, D. X. Cao, K. Cho, G. C. Bazan and
4 T. Q. Nguyen, *Advanced Energy Materials*, 2019, **9**, 1901438.
- 5 46. V. V. Brus, C. M. Proctor, N. A. Ran and T. Q. Nguyen, *Advanced Energy Materials*,
6 2016, **6**, 1502250.
- 7 47. J. Vollbrecht and V. V. Brus, *Advanced Electronic Materials*, 2020, **6**, 2000517.
- 8 48. H. M. Luong, S. Chae, A. Yi, K. Ding, J. Huang, B. M. Kim, C. Welton, J. Chen, H.
9 Wakidi, Z. Du, H. J. Kim, H. Ade, G. N. M. Reddy and T.-Q. Nguyen, *ACS Energy*
10 *Letters*, 2023, **8**, 2130-2140.
- 11 49. L.-W. Feng, J. Chen, S. Mukherjee, V. K. Sangwan, W. Huang, Y. Chen, D. Zheng, J. W.
12 Strzalka, G. Wang, M. C. Hersam, D. DeLongchamp, A. Facchetti and T. J. Marks, *ACS*
13 *Energy Letters*, 2020, **5**, 1780-1787.
- 14 50. I. Zonno, H. Zayani, M. Grzeslo, B. Krogmeier and T. Kirchartz, *Phys. Rev. Appl.*, 2019,
15 **11**, 054024.
- 16 51. G. Garcia-Belmonte, P. P. Boix, J. Bisquert, M. Sessolo and H. J. Bolink, *Solar Energy*
17 *Materials and Solar Cells*, 2010, **94**, 366-375.
- 18 52. N. Schopp, H. M. Luong, B. R. Luginbuhl, P. Panoy, D. Choi, V. Promarak, V. V. Brus
19 and T.-Q. Nguyen, *ACS Energy Letters*, 2022, **7**, 1626-1634.
- 20 53. C. M. Proctor, S. Albrecht, M. Kuik, D. Neher and T. Q. Nguyen, *Advanced Energy*
21 *Materials*, 2014, **4**, 1400230.
- 22 54. M. C. Heiber, T. Okubo, S. J. Ko, B. R. Luginbuhl, N. A. Ran, M. Wang, H. B. Wang,
23 M. A. Uddin, H. Y. Woo, G. C. Bazan and T. Q. Nguyen, *Energy & Environmental*
24 *Science*, 2018, **11**, 3019-3032.
- 25 55. N. A. Ran, J. A. Love, M. C. Heiber, X. C. Jiao, M. P. Hughes, A. Karki, M. Wang, V. V.
26 Brus, H. Wang, D. Neher, H. Ade, G. C. Bazan and T. Q. Nguyen, *Advanced Energy*
27 *Materials*, 2018, **8**, 1701073.
- 28 56. T. M. Burke, S. Sweetnam, K. Vandewal and M. D. McGehee, *Advanced Energy*
29 *Materials*, 2015, **5**, 1500123.
- 30 57. D. Bartesaghi, I. D. C. Pérez, J. Kniepert, S. Roland, M. Turbiez, D. Neher and L. J. A.
31 Koster, *Nat. Commun.*, 2015, **6**, 7083.
- 32 58. N. Tokmoldin, J. Vollbrecht, S. M. Hosseini, B. Sun, L. Perdigón - Toro, H. Y. Woo, Y.
33 Zou, D. Neher and S. Shoaee, *Advanced Energy Materials*, 2021, **11**, 2100804.
- 34 59. H. Cha, S. Wheeler, S. Holliday, S. D. Dimitrov, A. Wadsworth, H. H. Lee, D. Baran, I.
35 McCulloch and J. R. Durrant, *Advanced Functional Materials*, 2018, **28**, 1704389.
- 36 60. A. Karki, J. Vollbrecht, A. L. Dixon, N. Schopp, M. Schrock, G. N. M. Reddy and T.-Q.
37 Nguyen, *Advanced Materials*, 2019, **31**, 1903868.
- 38 61. G. Zhang, X.-K. Chen, J. Xiao, P. C. Y. Chow, M. Ren, G. Kupgan, X. Jiao, C. C. S.
39 Chan, X. Du, R. Xia, Z. Chen, J. Yuan, Y. Zhang, S. Zhang, Y. Liu, Y. Zou, H. Yan, K.
40 S. Wong, V. Coropceanu, N. Li, C. J. Brabec, J.-L. Bredas, H.-L. Yip and Y. Cao, *Nature*
41 *Communications*, 2020, **11**, 3943.
- 42 62. B. R. Luginbuhl, P. Raval, T. Pawlak, Z. Du, T. Wang, G. Kupgan, N. Schopp, S. Chae,
43 S. Yoon, A. Yi, H. Jung Kim, V. Coropceanu, J.-L. Brédas, T.-Q. Nguyen and G. N. M.
44 Reddy, *Advanced Materials*, 2022, **34**, 2105943.

- 1 63. R. L. B, P. Raval, T. Pawlak, Z. Du, T. Wang, G. Kupgan, N. Schopp, S. Chae, S. Yoon,
2 A. Yi, H. Jung Kim, V. Coropceanu, J. L. Bredas, T. Q. Nguyen and G. N. M. Reddy,
3 *Adv. Mater.*, 2022, **34**, e2105943.
- 4 64. J. Xin, H. Zhao, J. Xue, S. Seibt, B. A. Collins and W. Ma, *Solar RRL*, 2022, **6**, 2200819.
- 5 65. L. Zhu, M. Zhang, G. Zhou, T. Hao, J. Xu, J. Wang, C. Qiu, N. Prine, J. Ali, W. Feng, X.
6 Gu, Z. Ma, Z. Tang, H. Zhu, L. Ying, Y. Zhang and F. Liu, *Advanced Energy Materials*,
7 2020, **10**, 1904234.
- 8 66. A. Karki, J. Vollbrecht, A. L. Dixon, N. Schopp, M. Schrock, G. M. Reddy and T. Q.
9 Nguyen, *Adv. Mater.*, 2019, **31**, 1903868.
- 10 67. O. V. Mikhnenko, P. W. Blom and T.-Q. Nguyen, *Energy & Environmental Science*,
11 2015, **8**, 1867-1888.
- 12 68. M. T. Sajjad, A. Ruseckas and I. D. Samuel, *Matter*, 2020, **3**, 341-354.
- 13 69. L. Ye, Y. Xiong, S. Li, M. Ghasemi, N. Balar, J. Turner, A. Gadisa, J. Hou, B. T.
14 O'Connor and H. Ade, *Advanced Functional Materials*, 2017, **27**, 1702016.
- 15 70. E. Gann, A. T. Young, B. A. Collins, H. Yan, J. Nasiatka, H. A. Padmore, H. Ade, A.
16 Hexemer and C. Wang, *Review of Scientific Instruments*, 2012, **83**, 045110.
- 17 71. L. Ye, H. W. Hu, M. Ghasemi, T. H. Wang, B. A. Collins, J. H. Kim, K. Jiang, J. H.
18 Carpenter, H. Li, Z. K. Li, T. McAfee, J. B. Zhao, X. K. Chen, J. L. Y. Lai, T. X. Ma, J.
19 L. Bredas, H. Yan and H. Ade, *Nature Materials*, 2018, **17**, 253-260.
- 20 72. S. Mukherjee, C. M. Proctor, J. R. Tumbleston, G. C. Bazan, T. Q. Nguyen and H. Ade,
21 *Adv. Mater.*, 2015, **27**, 1105-1111.
- 22 73. L. Ye, S. Li, X. Liu, S. Zhang, M. Ghasemi, Y. Xiong, J. Hou and H. Ade, *Joule*, 2019, **3**,
23 443-458.
- 24 74. B. A. Collins, Z. Li, J. R. Tumbleston, E. Gann, C. R. McNeill and H. Ade, *Advanced*
25 *Energy Materials*, 2013, **3**, 65-74.
- 26 75. O. M. Awartani, B. Gautam, W. Zhao, R. Younts, J. Hou, K. Gundogdu and H. Ade,
27 *Journal of Materials Chemistry A*, 2018, **6**, 12484-12492.
- 28 76. X. G. Guo, N. J. Zhou, S. J. Lou, J. Smith, D. B. Tice, J. W. Hennek, R. P. Ortiz, J. T. L.
29 Navarrete, S. Y. Li, J. Strzalka, L. X. Chen, R. P. H. Chang, A. Facchetti and T. J. Marks,
30 *Nat. Photonics*, 2013, **7**, 825-833.
- 31 77. M. Tambasco, J. Lipson and J. S. Higgins, *Macromolecules*, 2006, **39**, 4860-4868.
- 32 78. L. Zhang, X. Zhu, D. Deng, Z. Wang, Z. Zhang, Y. Li, J. Zhang, K. Lv, L. Liu, X. Zhang,
33 H. Zhou, H. Ade and Z. Wei, *Adv. Mater.*, 2022, **34**, e2106316.
- 34 79. F. Etzold, I. A. Howard, N. Forler, D. M. Cho, M. Meister, H. Mangold, J. Shu, M. R.
35 Hansen, K. Müllen and F. Laquai, *Journal of the American Chemical Society*, 2012, **134**,
36 10569-10583.
- 37 80. N. C. Miller, E. Cho, M. J. Junk, R. Gysel, C. Risko, D. Kim, S. Sweetnam, C. E. Miller,
38 L. J. Richter, R. J. Kline, M. Heeney, I. McCulloch, A. Amassian, D. Acevedo-Feliz, C.
39 Knox, M. R. Hansen, D. Dudenko, B. F. Chmelka, M. F. Toney, J. L. Bredas and M. D.
40 McGehee, *Adv. Mater.*, 2012, **24**, 6071-6079.
- 41 81. M. Seifrid, G. Reddy, B. F. Chmelka and G. C. Bazan, *Nature Reviews Materials*, 2020,
42 **5**, 910-930.
- 43 82. A. L. Jones, C. H. Y. Ho, S. A. Schneider, J. Zhang, Y. Pei, J. Wang, X. Zhan, S. R.
44 Marder, M. F. Toney and F. So, *Chemistry of Materials*, 2022.

- 1 83. B. R. Luginbuhl, S.-J. Ko, N. A. Ran, H. Hu, S. M. Becwar, A. Karki, M. Seifrid, T.
2 Okubo, M. Wang, H. W. Ade, B. F. Chmelka, G. C. Bazan, G. N. Manjunatha Reddy and
3 T.-Q. Nguyen, *Solar RRL*, 2022, **6**, 2200135.
4